Effect of Mg microalloying on elevated-temperature creep resistance of Al-Cu 224 cast alloys

Peng Hu[1], Kun Liu[1*], Lei Pan[2] and X.-Grant Chen[1*]

[1] Department of Applied Science, University of Quebec at Chicoutimi, Saguenay (QC), Canada G7H 2B1

[2] Arvida Research and Development Centre, Rio Tinto Aluminum, Saguenay (QC), G7S 4K8, Canada

* Corresponding authors: kun.liu@uqac.ca (K. Liu), and xgrant_chen@uqac.ca (X.-G. Chen)

ABSTRACT

The influence of microalloying with Mg (0–0.36 wt%) on the elevated-temperature strength and creep resistance of Al-Cu 224 cast alloys was investigated. The Mg-containing alloys yielded finer and denser θ' precipitates after high-temperature stabilization (300 °C/100 h) than the Mg-free alloy, which improved the yield strength at both room temperature and 300 °C. Compressive creep tests were conducted at 300 °C over a wide range of the applied stresses (45–100 MPa). The results showed that the creep resistance increased with increasing Mg content at any fixed applied stress, and the alloy with 0.36 wt% Mg exhibited the best creep resistance among the four alloys studied. During creep deformation, the θ' precipitates continued to coarsen. However, Mg microalloying greatly stabilized the θ' precipitates in the matrix by slowing down the coarsening process. An obvious break was observed in the creep rate curves with different stress exponents (n). Below the break in the low-stress regime (LSR), stress exponent (n) was ~ 3, whereas it increased to 9-12 above the break in the high-stress regime (HSR). In the LSR, the creep was controlled by the dislocation climbing, and it transformed into the Orowan looping in the HSR.

Keywords: Al-Cu alloy; Mg addition; Elevated-temperature mechanical properties; Creep resistance; Creep mechanism

1. Introduction

Along with elevated-temperature strength, creep resistance is one of the most important considerations in the safety design of automotive engine components, which are projected to service at 300–350 °C, for enhancing the engine efficiency and fulfilling the emission standard requirements [1, 2]. Al-Cu cast alloys are widely used in the automotive and aircraft industries because they exhibit the highest mechanical strength among the various Al cast alloys [3]. However, the creep resistance of Al-Cu cast alloys decreases significantly because of the rapid coarsening of the main strengthening θ' phase at >250 °C [4-6]. Hence, it is necessary to improve the creep resistance for critical applications at high temperatures.

Several approaches have been proposed to improve the creep resistance of aluminum alloys at high temperatures, such as (i) stabilizing the precipitates to avoid

coarsening at high temperatures in precipitation-hardening alloys, (ii) introducing thermally stable dispersoids in the matrix, and (iii) introducing secondary phases at the grain boundary to impede grain boundary sliding [6, 7].

Increasing the high-temperature stability of precipitates has been proven to be an effective method for improving creep resistance [6, 8-13]. Several studies have reported that the addition of Sc and Zr to Al-Cu alloys promotes the formation of fine and densely distributed θ'' and θ' precipitates and suppresses the coarsening of these precipitates at high temperatures [8, 9]. In addition, the formation of nano-sized $Al_3(Sc, Zr)$ dispersoids, which are thermally stable at 300–350 °C, can pin the dislocations and show excellent elevated-temperature creep resistance [10-12]. Other studies reported that the addition of Mn and Zr can prevent the transformation of the main strengthening θ' phase to the equilibrium θ phase up to 350 °C by segregating Mn and Zr at the precipitate interfaces, enhancing the creep resistance [13, 14]. Yao et al. [6] reported that La-added Al-Cu cast alloys exhibited good thermal stability and creep resistance owing to the formation of the $Al_{11}La_3$ phase, which inhibited grain boundary migration and dislocation movement during creep deformation. Recently, Rakhmonov et al. [2] investigated the effect of Mg microalloying on the elevated-temperature mechanical properties of Al-Cu 224 cast alloys. The results showed that the addition of Mg could significantly promote the precipitation of θ' strengthening phase and hence improve the elevated-temperature mechanical properties, which are expected to have the benefit on the creep resistance of Al-Cu alloys.

To study the creep behavior of metals, creep tests with a constant load and a fixed temperature in tensile or compression creep are often conducted, and the creep strain is plotted as a function of time. A typical creep curve exhibits three creep stages: the primary creep stage, the secondary creep stage, which is often referred to as the steady-state creep, and the tertiary creep stage [7, 15]. The minimum creep rate in the steady-state stage is often used to characterize creep properties. The relationship between the minimum creep rate (ε) and applied stress (σ) is described by the classical power-law equation [5, 6, 16]:

$$\varepsilon = A\sigma^n \exp\left(\frac{-Q}{RT}\right) \tag{1}$$

where A is the material constant, n is the stress exponent, Q is the apparent activation energy, T is the absolute temperature (K), and R is the ideal gas constant. The value of stress exponent n is closely related to the creep mechanism, as revealed in previous studies [17-19]. However, precipitation-hardening alloys have exhibited significantly different creep behaviors. Some reports have shown that precipitation-hardened alloys display higher stress sensitivity of creep rate than pure metals [20-22]. Moreover, a pronounced break has been observed in the creep curves of some precipitation-hardened alloys [20, 21, 23-26]. The different slopes below and above the break indicated different creep mechanisms, which was confirmed in well-known high-temperature γ-hardened Ni-based alloys [20, 21]. These features were also observed in Al-Mn alloys [23], Cu-Co alloys [24], Sn-Ag/Cu solders [25] and Al-Fe, V, Si alloys [26]. Surprisingly, few studies have focused on the creep behavior over a range of applied stresses in the precipitation-strengthened Al-Cu alloys [14, 27-29].

In our previous works [2, 30], we found that microalloying with Mg could promote the precipitation of θ′ and enhance the elevated-temperature mechanical properties in Al-Cu 224 alloys. However, above a certain Mg level (0.19 wt.% in [2] and 0.24 wt.% in [30]), the elevated-temperature strength declined with increasing Mg level. In the present work, we extended the Mg levels (0 to 0.36 wt%) to study the effect of Mg microalloying on the creep resistance of Al-Cu 224 alloys over a wide range of applied stress (45–100 MPa), in order to better assess the potential of those Al-Cu alloys for elevated temperature applications. The microstructures before and after creep deformation were examined using scanning and transmission electron microscopies. Different creep mechanisms were explored in relation to the stress exponents and microstructure evolution.

2. Experimental procedures

Four Al-Cu 224 alloys with varying Mg contents, 0–0.36 wt%, were prepared. The alloys were melted in an electric resistance furnace and degassed with pure Argon for 10 min, and then grain-refined with an Al-5Ti-1B master alloy. The molten metal was cast into a permanent wedge mold. The pouring temperature was 720 °C and the preheating temperature of the wedge mold was 250 °C. Chemical compositions of the alloys analyzed using optical emission spectroscopy are listed in Table 1. A rectangular sample cut from the bottom of the wedge casting was used in the investigations. T7 heat treatment was first applied to all cast samples; it included the following steps: 1) a two-step solution treatment conducted first at 495 °C for 2 h and then at 528 °C for 10 h, followed by water quenching; 2) artificial aging at 200 °C for 4 h. To study the elevated-temperature strength and creep behavior, all T7-treated samples were further exposed at 300 °C for 100 h to stabilize the microstructure, which was designated as T7A treatment.

Table 1. Chemical composition of 224 cast alloys (wt%)

Alloy	Cu	Mn	Mg	Si	Fe	Ti	V	Zr	Al
0Mg	4.68	0.34	**0.01**	0.04	0.11	0.17	0.21	0.14	Bal.
0.12Mg	4.69	0.34	**0.12**	0.04	0.11	0.17	0.21	0.15	Bal.
0.24Mg	4.71	0.36	**0.24**	0.04	0.08	0.15	0.18	0.14	Bal.
0.36Mg	4.86	0.35	**0.36**	0.05	0.12	0.17	0.21	0.14	Bal.

The compressive tests at room temperature and 300 °C were conducted using a Gleeble 3800 thermo-mechanical simulator unit with a fixed strain rate of 10^{-3} s^{-1} to obtain the stress-strain curves. The 0.2% offset yield strengths of the experimental alloys were determined from the corresponded stress-train curves. Cylindrical specimens (diameter = 10 mm, height = 15 mm) were machined for compressive testing. At least three samples were tested for each condition, and their averages were calculated. Compressive creep tests were performed on the T7A-treated samples at 300 °C using the same cylindrical sample size used in the compressive yield strength tests. Seven different stresses were applied in the creep tests for each alloy, varying from 45 to 100 MPa. At least three tests were conducted for each creep condition and the average value was used.

The microstructures of all experimental alloys were characterized using optical microscopy (OM), scanning electron microscopy (SEM), and transmission electron microscopy (TEM). To reveal the grain structure, the polished samples were etched using Keller's reagent. At least 500 grains were quantified using ImageJ software for each alloy to obtain the average grain size. To observe the microstructural evolution during creep deformation, the samples were quenched at different stages and etched with Keller's reagent for SEM observation. The samples before and after the creep test were prepared for TEM observation to study precipitate evolution. The creep TEM samples were cut perpendicular to the compressive axis at the center. All TEM samples were ground to approximately 40–60 μm and then subjected to a twin-jet electrochemical process at -20 °C with a voltage of 20 V in a solution comprising 200 mL methanol and 75 mL nitric acid. TEM was performed at 200 kV to characterize the precipitates, including the selected area diffraction pattern (SADP). TEM foil thickness was measured using the two-beam convergent beam diffraction pattern (CBED) [31]. Quantification of the θ'-Al_2Cu precipitates, such as the number density and volume fraction, was conducted on several TEM images using a previously described method [32, 33]. At least 1000 precipitates were quantified for each alloy and condition to obtain the average values.

3. Results

3.1 Microstructure

Fig. 1 shows the typical as-cast and T7A-treated microstructures of the 0.12Mg alloy. The as-cast grain structure comprised fine equiaxed grains, and the average grain size of all the experimental alloys was ~40 μm, irrespective of the different Mg contents (Fig. 1a). After T7A treatment (Fig. 1b), all the experimental alloys displayed a similar microstructure, comprising α-Al grains, Al_3(Ti, Zr, V), and Al_7Cu_2(Fe, Mn) intermetallic. The backscatter SEM image indicates that the platelet Fe-rich phase, Al_7Cu_2(Fe, Mn) (bright phase indicated by the red arrows), was mainly located at the grain boundaries, while the roundish Al_3(Ti, Zr, V) (dark phase indicated by the red arrows) was randomly distributed in the matrix.
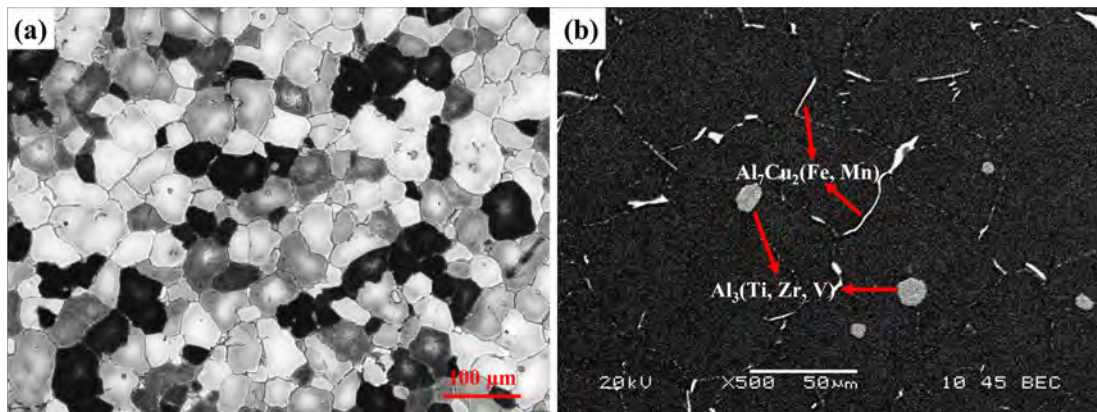

Fig. 1 Typical microstructure of 0.12Mg alloy: (a) OM image showing the as-cast grain structure and (b) backscatter SEM image showing two intermetallic phases after T7A.

The bright-field TEM images observed along the $<001>_{\alpha\text{-Al}}$ of the experimental alloys after T7A treatment are shown in Fig. 2. The microstructure of the Al-Cu 224 alloys after T7 aging generally comprised a mixture of fine θ'' and θ' strengthening phases [2, 30, 34]. After stabilization at 300 °C for 100 h (T7A), the precipitate microstructure was predominantly θ' in all the investigated alloys, which was confirmed by the characteristic spots and streaks of θ', shown by the white arrows in the SADP (Fig. 2f) [8]. However, their characteristics varied with Mg content; the θ' plates in the Mg-containing alloys (Fig. 2b-d) were finer and denser than those in the Mg-free alloy (Fig. 2a), which is further confirmed by the quantitative results listed in Table 2. For example, the thickness and length decreased from 14.7 nm and 286.2 nm in the 0Mg alloy to 8.9 nm and 82.7 nm in the 0.36Mg alloy, respectively. Meanwhile, the number density of θ' significantly increased from 8.4×10^{-8} to 9.8×10^{-7} nm^{-3}.

It is also observed that with increasing Mg content, another phase (cubic σ-$Al_5Cu_6Mg_2$) started to precipitate in the Al matrix, confirmed by TEM-EDS results. Up to 0.24%Mg, there was only a trace amount of cubic σ-$Al_5Cu_6Mg_2$ detectable. However, with 0.36% Mg addition, the number of cubic σ-$Al_5Cu_6Mg_2$ particles significantly increased (Fig. 2e). The formation of σ-$Al_5Cu_6Mg_2$ would consume the Cu solutes in the Al matrix leading to the decrease of volume fraction of θ' in 0.36Mg alloy.

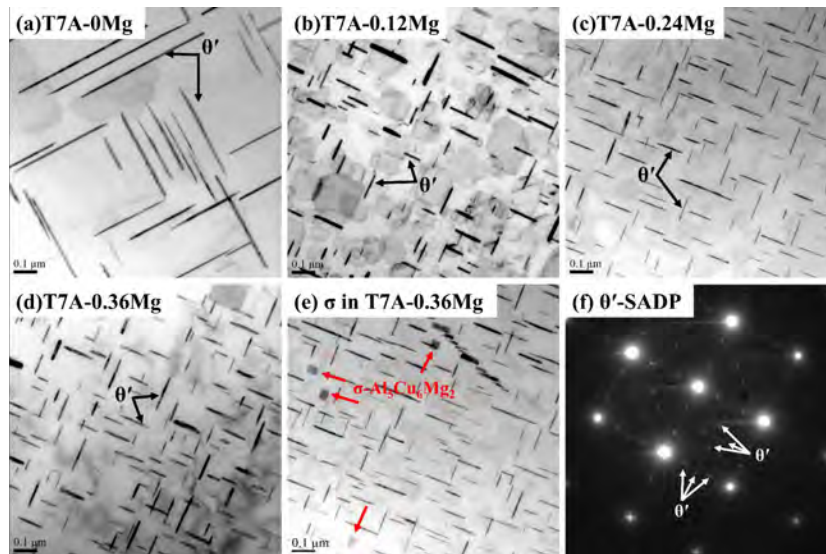**Fig. 2** Bright-field TEM images of experimental alloys after T7A: (a) 0Mg, (b) 0.12Mg, (c) 0.24Mg, (d) 0.36 Mg alloy and (e) showing σ-$Al_5Cu_6Mg_2$ in 0.36Mg alloy, and (f) displaying the typical SADP of θ' in (a-d) viewed along $<001>_{\alpha\text{-Al}}$.

Table 2 Summary of quantitative TEM results of θ′ phase after T7A treatment.

Alloy	Quantified particles	Length (nm)	Thickness (nm)	Number density (nm^{-3})	Volume fraction (%)
0Mg		286.2±149.0	14.7±4.8	8.4×10^{-8}	6.1
0.12Mg	θ′	159.6±96.5	12.4±5.6	2.7×10^{-7}	5.2
0.24Mg		97.6±34.5	9.2±2.8	7.1×10^{-7}	4.7
0.36Mg		82.7±33.5	8.9±3.4	9.8×10^{-7}	4.1

3.2 Mechanical properties

Compressive yield strengths of the alloys at room temperature and 300 °C after T7A treatment are shown in Fig. 3. The yield strength at room temperature increased from 197 MPa in the Mg-free (0Mg) alloy to 212 MPa in the 0.12Mg alloy and further to 256 MPa in the 0.24Mg alloy, and then, it decreased to 219 MPa in the 0.36Mg alloy. A similar trend was found for the yield strength at 300 °C, where it increased from 122 MPa in the Mg-free alloy to 142 MPa in the 0.24Mg alloy, and then decreased to 134 MPa in the 0.36Mg alloy. The decrease of the yield strength in the 0.36Mg alloy at both room temperature and 300 °C could be attributed to the precipitation and the increased number of cubic σ-Al$_5$Cu$_6$Mg$_2$ particles, which consumed the Cu solutes in the Al matrix leading to the decrease of volume fraction of θ′ precipitates. Clearly, the Mg addition generally improves the yield strength at room temperature as well as at 300 °C after T7A treatment, and the alloy with 0.24% Mg showed the best mechanical strength.
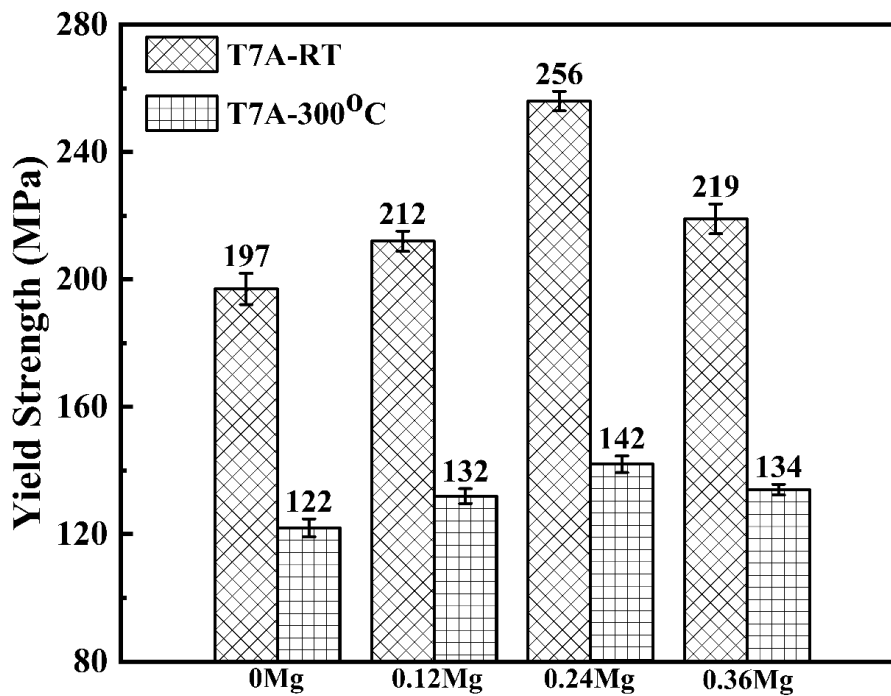
Fig. 3 Compressive yield strength of 224 experimental alloys at room temperature and 300 °C after T7A heat treatment.

3.3 Creep behavior

Fig. 4 shows the typical compressive creep curves of the experimental alloys examined at 300 °C for up to 100 h at 65 MPa and 95 MPa. At low applied stresses (for example, 65 MPa), the creep curves displayed two typical stages: primary stage and secondary (quasi-steady) stage. Due to work hardening, the creep rate in the primary stage continued to decrease (Fig. 4a and c). With further deformation, the creep rate finally reached the lowest level and barely changed with increasing time (Fig. 4c) due to the balance between work hardening and thermal softening. The constant creep rate in the quasi-steady stage is often referred to as the minimum creep rate. The minimum creep rates in this study are the average values measured from the quasi-steady stage. At high applied stresses (for example, 95 MPa), a tertiary stage appeared followed by the quasi-steady stage (Fig. 4b and d), in which the creep strain increased sharply (Fig. 4b) and the creep rate increased gradually. The creep deformation in the tertiary stage becomes unstable, accompanied by microstructure failure (breakdown of the intermetallic components and grains and occurrences of cracking), which will be discussed later in detail. This creep behavior was also observed in another study [35].
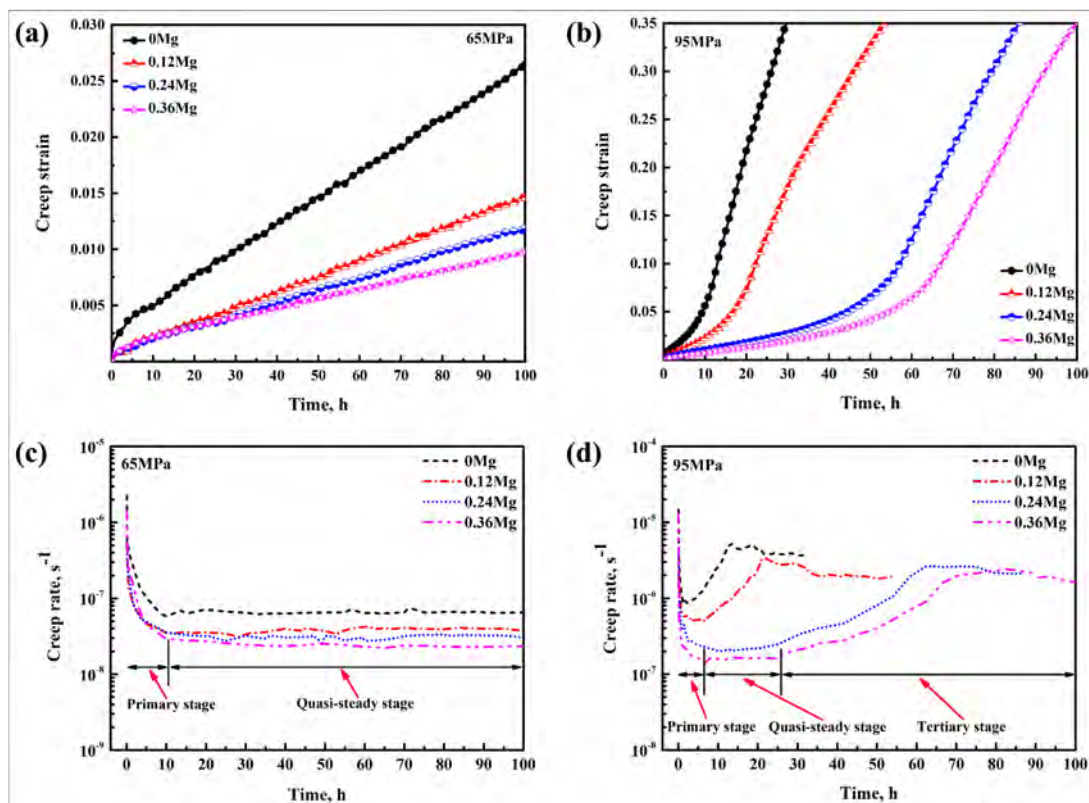

Fig. 4 Typical creep curves of experimental alloys at (a) 65 MPa and (b) 95 MPa, and the creep rate curves at (c) 65 MPa and (d) 95 MPa. The schematic indication of the creep stages in Fig. 4d is based on 0.24Mg and 0.36Mg creep rate curves.

The minimum creep rates as a function of the applied stress are logarithmically displayed in Fig. 5. For all four alloys tested, two regimes were observed based on the slope of the creep rate vs. applied stress curves (for example, low-stress regime (LSR)

= 45–75 MPa, high-stress regime (HSR) = 90–100 MPa), and they were separated by the break of the overall curves. In Fig. 5, a linear fit of the double-logarithmic plot was applied to each regime to calculate the stress exponents corresponding to the two regimes. For all the alloys, the slope of the creep rate curves changed sharply from the LSR to the HSR. An obvious break in the creep rate curves was also observed for various precipitation-hardened alloys [20, 21, 23-26]. In the LSR, n = ~3 for all the experimental alloys, whereas it changed considerably to >9 after an applied stress of 75 MPa in the HSR. With increasing Mg content, the minimum creep rates decreased in the LSR as well as HSR, indicating enhanced creep resistance due to Mg addition. The 0.36Mg alloy exhibited the lowest minimum creep rate, and hence, the best creep resistance at 300 °C. The creep curves of the four alloys at different applied stresses as well as their creep rates in the secondary stage are shown in Fig. S1 and Table S1 (Supplementary Materials).
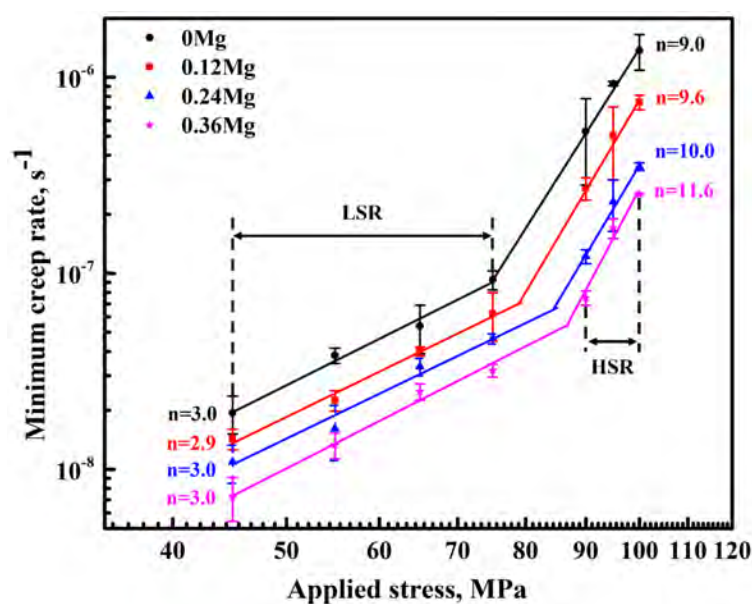

Fig. 5 Minimum creep rate as a function of applied stress (logarithmic scale) for different Mg-containing alloys at 300 °C.

The total strain after 100 h of creep and the time to failure were also used to characterize the creep properties of the LSR and HSR, respectively (Fig. 6). In the LSR, the total strain increased with increasing applied stress; however, the total strain decreased remarkably with increasing Mg level (Fig. 6a) at a given stress. For instance, the average total strain decreased from 0.022 for the 0Mg alloy to 0.008 for the 0.36Mg alloy at 65 MPa applied stress. In the HSR, the time to failure is the creep duration before the tertiary creep. During creep at high applied stresses, the 0Mg alloy quickly entered the tertiary creep (in <10 h), indicating poor creep resistance. In contrast, the time to failure of the Mg-containing alloys was much longer (Fig. 6b). The results of the total strain and the time to failure also confirmed that the creep resistance improved with increasing Mg content, and the 0.36Mg alloy exhibited the best creep resistance among the four alloys studied.

It is worthwhile to mention that for aluminum alloys in elevated temperature applications, the elevated-temperature strength and creep resistance are two important design aspects to be considered. Although the 0.36Mg alloy showed the highest creep resistance, the 0.24Mg alloy exhibited the best mechanical strength and second highest creep resistance among the four alloys studied. Based on the two aspects above, the 0.24Mg alloy is considered to be the optimum one for the overall performance at elevated temperatures.
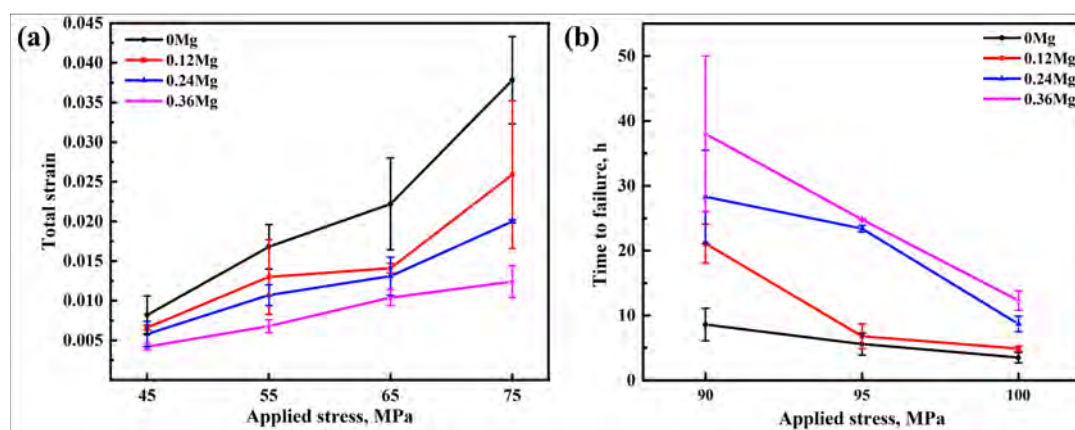
Fig. 6 (a)Total strain after 100 h and (b) the time to failure as function of the applied stress in experimental alloys.

As observed in Fig. 4(b) and 4(d), there was a distinct change in the creep rate in the tertiary stage of creep, where it initially increased sharply and then slowed down to an approximately stable value, as schematically shown in Fig. 7(a). To reveal the different failure modes in the tertiary stage of creep, the creep samples were interrupted at different phases of the tertiary stage and quenched with water, and the quenched microstructures were observed. For the 0Mg alloy, at the beginning of the tertiary stage, several broken intermetallics on the grain boundaries and a few cracks in the grain interiors were observed, as indicated by the white arrows in Fig. 7(b). Thus, the sliding of the broken grains under high applied stress caused a sharp increase in the creep rate, and their failure modes were believed to be the sliding of the broken grains. As the creep deformation continued to the middle of the tertiary stage (Fig. 7(c)), small crush bands were formed by the severe breakage of intermetallics and grains. Further creep deformation caused the crush bands and the broken grains to merge (Fig. 7(d)), slowing the creep rate and becoming relatively stable. After the sliding of the broken grains, the failure mode was the merging of the crush bands and the broken grains.
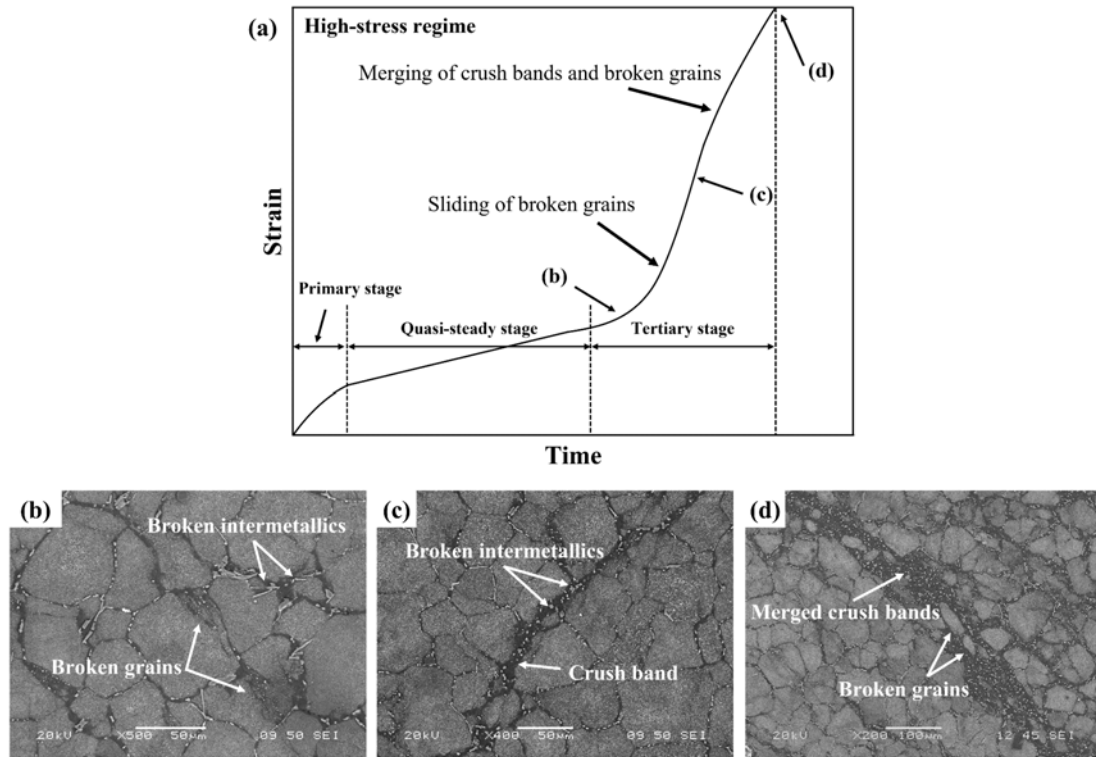
Fig. 7 (a)Schematic compressive creep stages in the high-stress regime and the failure modes in the third stage of creep. The microstructures of crept 0Mg alloy quenched at (b) beginning of the third stage, (c) middle of the third stage and (d) end of the creep test.

The microstructural evolution in the tertiary stage of the HSR indicates the existence of severe plastic deformation during creep. Unlike the LSR in the elastic deformation zone, the HSR was in the elastic-plastic deformation zone before reaching the engineering yield stress, as illustrated by the compressive stress-strain curves in Fig. 8. During creep in the HSR, plastic deformation was activated to some extent. It took much longer for the Mg-containing alloys to reach the tertiary stage (Fig. 4(d) and 6(b)), and these alloys suffered less plastic deformation compared to the base alloy. The grain boundary structures revealed that large and sparse particles occurred on the grain boundaries of the 0Mg alloy (Fig. 9(a)), while there were smaller and denser particles covering almost the entire grain boundaries in the Mg-containing alloys (0.24Mg alloy, Fig. 9(b)). These particles were identified as the equilibrium θ-Al$_2$Cu phase according to the SEM-EDS results (Al-69.7 at%, Cu-30.3 at%) and their morphologies. The addition of Mg possibly promoted the formation of θ-Al$_2$Cu particles on the grain boundaries and inhibited coarsening during T7A treatment, although the mechanism is not yet well understood. The uniformly distributed θ-Al$_2$Cu particles and their high coverage on the grain boundaries enhance the stability of the grain structure and inhibit grain boundary migration during plastic deformation [14].
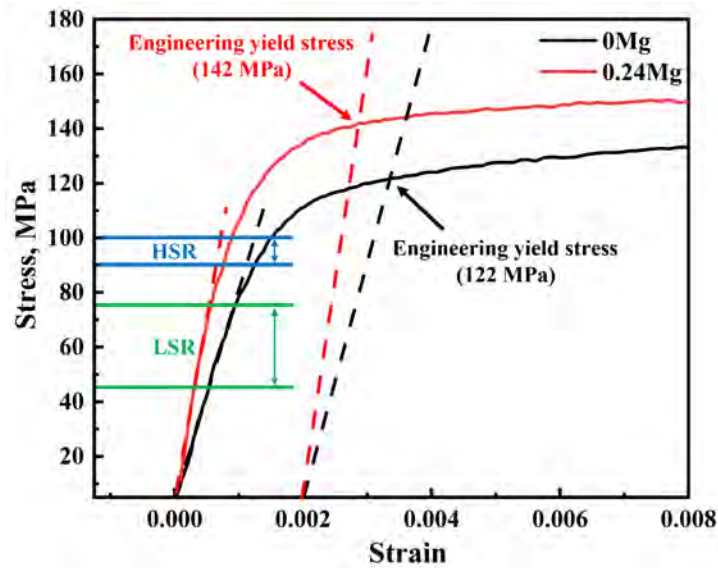
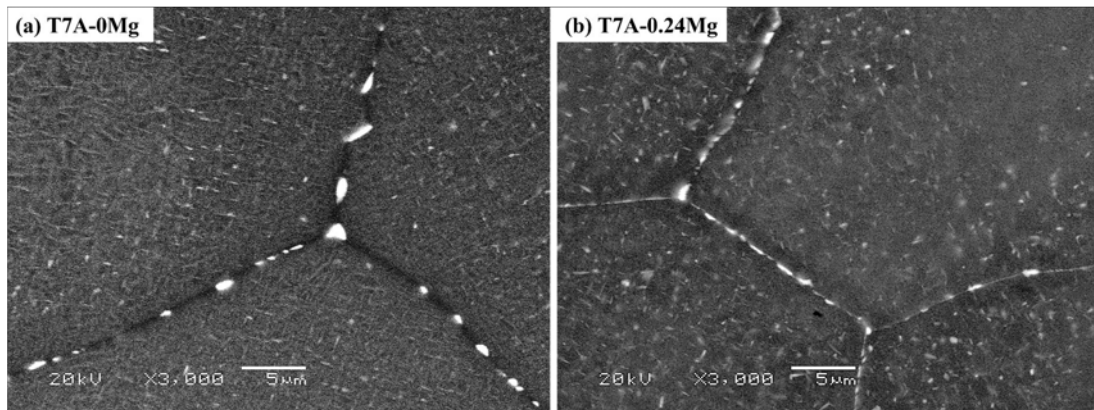**Fig. 8** Compressive stress-strain curves of 0Mg and 0.24Mg alloys tested at 300 °C.

Fig. 9 Backscattered electron image of the grain boundary structure covered by θ-Al₂Cu particles: (a) 0Mg alloy and (b) 0.24Mg alloy after T7A condition. Note the higher coverage of the grain boundaries by particles in 0.24Mg than 0Mg alloy.

3.4 Precipitate evolution after creep deformation

The precipitate evolution after creep deformation was examined by TEM, and typical bright-field TEM images along $<001>_{\alpha\text{-Al}}$ are shown in Fig. 10. Here, the applied stresses of 65 MPa and 90 MPa were selected to represent the precipitates in the LSR and HSR, respectively. The selected diffraction patterns (not shown here) confirmed that the dominant precipitate after the creep test in both the LSR and HSR was still θ′ for all the experimental alloys. A few equilibrium θ particles were also observed after the creep process. The quantitative results are presented in Table 3. Compared with the θ′ plates before creep (Fig. 2 and Table 2), the θ′ precipitates after creep became longer and thicker. Take 0Mg alloy as example, the length and thickness after creep at 65 MPa increased 13.2% and 12.9%, respectively. High external stress increased the size of the θ′ precipitates. For example, when the applied stress increased from 65 to 90 MPa, the length and thickness of the θ′ plates increased from 324 and 17 nm to 359 and 20 nm,

representing an increase of 10.8 % and 19.3%, respectively, in the 0Mg alloy. However, for the Mg-containing alloys, the length and thickness of θ′ increased to a lesser extent. In addition, the number density of θ′ in all the experimental alloys decreased when the stress increased from 65 to 90 MPa. Again, the Mg-containing alloys showed a much higher number density of θ′ than the Mg-free base alloy, which was one order of magnitude higher. The TEM results indicated that the Mg-containing alloys have a better coarsening resistance of θ′ precipitates during creep deformation relative to the Mg-free alloy.
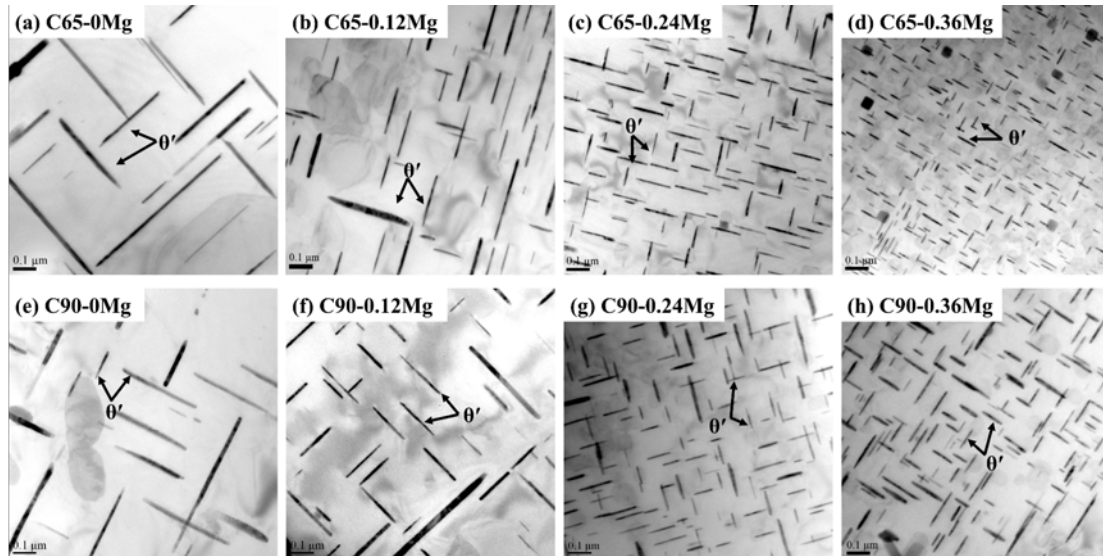

Fig. 10 Bright-field TEM images viewed along <001>$_{\alpha\text{-Al}}$ of all the experimental alloys after creep for 100 h at the applied stress of 65 MPa (C65) and 90 MPa (C90).

Table 3 Summary of quantitative TEM results of θ′ precipitates after creep

Alloy	Quantified particles	Condition (Applied stress)	Length (nm)	Thickness (nm)	Number density (nm^{-3})	Volume fraction (%)
0Mg		C65	324.1±139.4	16.6±6.6	4.0×10^{-8}	7.6
		C90	359.1±180.9	19.8±7.9	3.5×10^{-8}	8.9
0.12Mg		C65	221.0±89.3	15.8±5.4	1.2×10^{-7}	6.4
	θ′	C90	234.0±81.0	16.6±6.4	1.0×10^{-7}	7.3
0.24Mg		C65	101.5±37.8	9.9±3.5	4.2×10^{-7}	4.9
		C90	120.0±53.1	12.7±4.6	3.7×10^{-7}	5.2
0.36Mg		C65	89.2±46.7	9.7±4.0	6.8×10^{-7}	4.0
		C90	96.4±38.9	11.4±3.2	5.9×10^{-7}	5.0

4. Discussion

4.1 Effect of Mg on the coarsening of θ′ precipitates during thermal exposure and creep process

In our previous study [2, 30], it is observed that after the T7 aging treatment, the main precipitates in the 0Mg alloy were θ″, whereas a mixed microstructure of θ′ and

θ″ as strengthening phases was found in the Mg-containing alloys. After stabilizing at 300 °C for 100 h (T7A treatment) in the present study, all precipitation microstructures of the four alloys transformed to θ′ precipitates as the predominant strengthening phase, accompanied by coarsening during stabilization (Fig. 2). The θ″ plates in the 0Mg alloy dissolved quickly and formed fewer and thicker θ′ particles, whereas the Mg-containing alloys mainly experienced lateral growth at the expense of small θ″ precipitates during the high-temperature stabilization at 300 °C. Clearly, Mg microalloying increased the coarsening resistance of the θ′ precipitates, resulting in a finer size and a higher number density of the θ′ precipitates than in the 0Mg alloy after T7A treatment (Table 2). With increasing Mg content, the θ′ precipitates became finer and denser in the matrix.

During creep deformation, under external stress and high temperature, the θ′ precipitates continued to coarsen in all the Mg-free and Mg-containing alloys; however, the dominant precipitates were still θ′ particles after the creep process (Fig. 10), which generally provided a reasonable creep resistance in the LSR (Fig. 4a). The high applied stress resulted in severe coarsening of θ′ precipitates as a high number density of dislocations would be generated during creep deformation that promoted the element diffusion and hence the coarsening of precipitates. This accelerated the creep progress in the HSR (Fig. 4b). The TEM results (Fig. 10) revealed that the Mg-containing alloys exhibited a higher coarsening resistance of θ′, even under external stress during creep exposure, than the Mg-free alloy. Fig. 11 shows a comparison of the precipitate characteristics before and after creep for the 0Mg and 0.24Mg alloys. The 0Mg alloy exhibited coarse precipitates prior to creep, and the precipitates became much coarser after creep, whereas the 0.24Mg alloy had fine precipitates before creep and the coarsening during creep increased to a much lesser extent. This indicates that Mg microalloying greatly stabilized the θ′ precipitates in the matrix by slowing down the coarsening process of the precipitates during either thermal exposure (T7A) or high-temperature creep deformation, which provided improved creep resistance in the Mg-containing alloys.
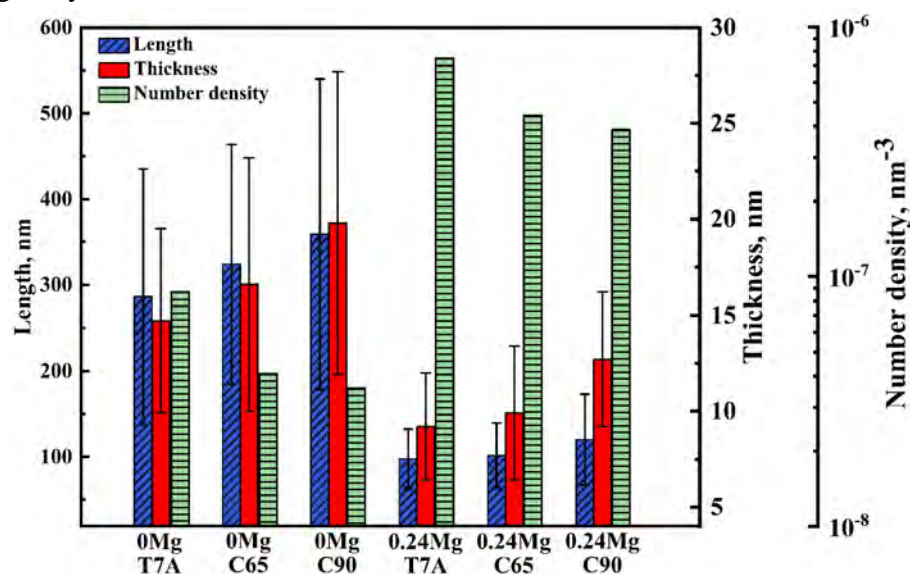

Fig. 11 Characteristics of precipitates after creep deformation from T7A-treated 0Mg alloy and 0.24Mg alloy

4.2 Creep mechanism

The precipitation-hardened Al-Cu alloys in this study displayed different creep behaviors than pure aluminum. An obvious break was observed in the creep rate-stress curves (Fig. 5), where the n was approximately 3 below the break, while it was >9 above the break, which is much greater than the value of 4.4 in pure aluminum [16, 36]. It has been reported that the stress exponent is related to the creep mechanism [17-19]. Unlike pure metals and solid-solution alloys, precipitation-hardened alloys containing the break showed a different relationship between the stress exponent and creep mechanism. When the value of n is much higher than 5 (above the break), the dominant creep mechanism is believed to be Friedel cutting (coherent particles) or Orowan bypassing (semi-coherent and incoherent particles) [20, 21, 23, 25]; whereas a value of n at 3–4 indicates that dislocations can bypass the precipitates by thermally-activated climbing [16, 20, 21, 37]. A schematic representation of the interaction between dislocations and the precipitates is shown in Fig. 12 [38, 39].
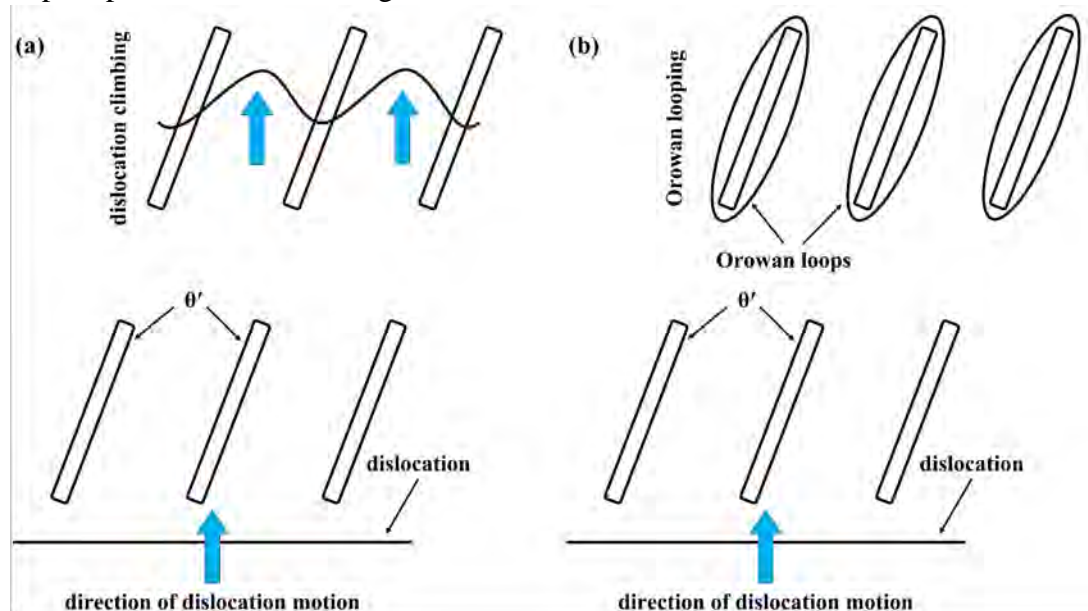

Fig. 12 Schematic representation of (a) dislocation climbing [38] and (b) Orowan looping [39].

A chart of the minimum creep rate, $\dot{\varepsilon}^{1/n}$, versus the applied stress is plotted in Fig. 13, where the value of $n = 3$ gives the best linear fit in the LSR for all the experimental alloys. Hence, the creep deformation for all experimental alloys in the LSR was assumed to be controlled by dislocation climbing. Threshold stress was not observed in the LSR for all the experimental alloys when the data were extrapolated to $\dot{\varepsilon} = 0$ (see Fig. 13). Several studies also confirmed that threshold stress was not found in dispersion-hardened Al-Mg alloys [40], Al-Fe, V, Si alloy [26] and γ'-hardened Ni-base alloy [20, 21]. In the HSR, the creep behavior of all the alloys was dominated by Orowan looping. In this case, extrapolating the data to $\dot{\varepsilon} = 0$ in the HSR can yield the experimental Orowan loop stress, as previously found [20, 23, 25, 26]. An upward trend was observed as the Mg content increased from 0 to 0.36 wt.%: 63 MPa (0Mg), 65 MPa

(0.12Mg), 66 MPa (0.24Mg) and 72 MPa (0.36Mg). Meanwhile, the stress for the Orowan loop can be calculated using the following equation [21, 25]:

$$\sigma_{Or} = \frac{0.4Gb}{\pi\lambda} \cdot \frac{ln(d/b)}{(1-\nu)^{\frac{1}{2}}} \tag{2}$$

where λ is the interparticle spacing, d is the average particle diameter, b is Burger's vector, ν is Poisson's ratio, and G is the shear modulus. Based on Eq. 2, the theoretical Orowan looping stresses were calculated as 66 MPa (0Mg), 67 MPa (0.12Mg), 70 MPa (0.24Mg) and 72 MPa (0.36Mg), which is in good agreement with the experimental data shown in Fig. 13.
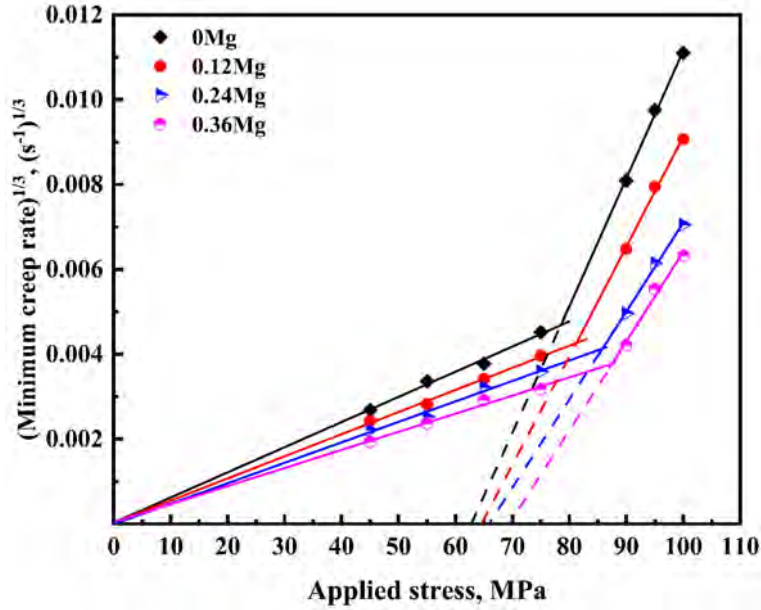

Fig. 13 Plot of $\dot{\varepsilon}^{1/n}$ vs applied stress, using a value of 3 for n.

The interactions between the precipitates and dislocations in the quasi-steady stage were observed using TEM. Fig. 14(a) and 14(b) show typical weak-beam dark-field TEM images viewed along <001>$_{\alpha\text{-Al}}$ of the 0.24Mg alloy at the quasi-steady stage under applied stresses of 65 and 95 MPa. In the LSR (65 MPa), some dislocation segments climbed above the precipitates, as indicated by the red arrows in Fig. 14(a). Characteristics of Orowan looping, such as closed loops and dislocation pairs [20] were not observed. Hence, it is suggested that the creep mechanism in the LSR is dislocation climbing. In the crept HSR sample (Fig. 14(b)), some dislocation loops on the broad face of the θ′ plates were observed, which was also previously confirmed [41]. Fig. 14(c) provides another example of 0Mg alloy at the quasi-steady stage under an applied stress of 95 MPa, in which many dislocation loops are left on the θ′ plates. Therefore, it is reasonable to believe that Orowan looping is the dominant creep mechanism in the HSR. The thinner and denser θ′ particles observed in the Mg-containing alloys (Fig. 2) exhibited a higher hindering effect on dislocation climbing and Orowan looping during creep deformation than the Mg-free alloy, resulting in a higher creep resistance.
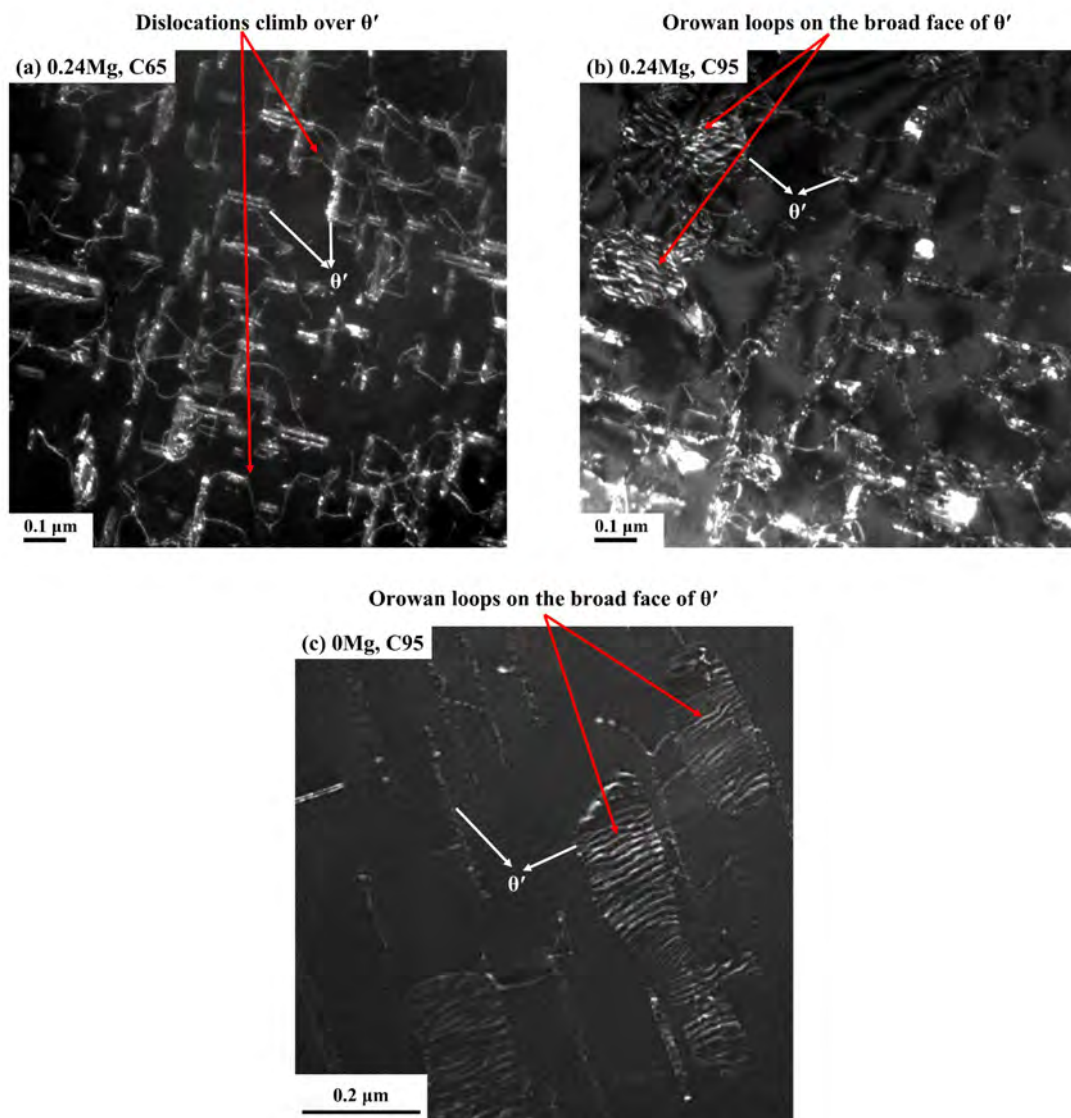
Fig. 14 Weak-beam TEM images viewed along $<001>_{\alpha\text{-Al}}$ of crept samples quenched at the steady-state stage, (a) 0.24Mg alloy, 65 MPa (LSR) and (b) 0.24Mg alloy, 95 MPa (HSR) and (c) 0Mg alloy, 95 MPa (HSR).

As mentioned above, when the applied stress was sufficiently high to overcome the Orowan loop stress provided by the semi-coherent θ′ precipitates, Orowan looping dominated the creep deformation in the HSR. In the LSR, the applied stress is insufficient to operate by Orowan looping, and dislocations bypass the precipitates by thermally activated climbing. Interestingly, in the tertiary stage in the HSR, the active creep mechanism of the 224 alloys transferred from micro-scale (Orowan looping) to macro-scale (grain structure collapsing and sliding). In general, the addition of Mg enhanced the creep resistance of the Al-Cu 224 cast alloys through the stabilization of the θ′ precipitates during thermal exposure and creep owing to the great hindering effect of the dislocation motion in the matrix (dislocation climbing and Orowan looping). Furthermore, the formation of the θ-Al$_2$Cu particles with high coverage on the grain

boundaries in the Mg-containing alloys provided supplementary support for creep resistance by inhibiting grain rotation and grain boundary migration, particularly in the HSR.

4.3 Comparison of the creep data of various aluminum alloys

Fig. 15 provides the comparison of the minimum creep rates of several alloys in Al-Cu-(Mg) alloy family. All the creep tests were performed at 300 °C. Compared to a conventional Al-Cu 206 alloy [14], the 224 cast alloys exihibted much low creep rates, indicating an excellent thermal stablity and creep resistance. The creep data of two high-Mg-containing Al-Cu-Mg alloys via powder metallurgical route are also included in Fig. 15. The Al-4.4Cu-1.47Mg alloy with higher Mg level [27] exhibited a higher creep rate than the Al-3.7Cu-1.3Mg alloy with lower Mg level [28], but both alloys had faster creep rates (lower creep resistance) than 224 alloys studied in the present work. In recent years, several studies have explored the addition of transistion elements (particlurary Zr, Mn, Sc, etc.) to improve the thermal stability of θ' strengthening phase and hence enhance the elevated-temperature properties in Al-Cu alloys [2, 12-14, 34]. Because our 224 alloys also contained the transistion elements (Zr, V, Ti and Mn, see Table 1), the creep rates of the 0Mg alloy were almost the same as those of the newly developed ACMZ (Al-6.1Cu-0.42Mn-0.15Zr) alloy [29]; both alloys were at very levels of the creep rates, which were even lower than the Sc-containing Al-2.5Cu alloy [12]. However, the present work domostrated that the creep resistance of 224 alloys could be further improved by Mg microalloying. The 0.36Mg alloy exhibted one of the lowest creep rates (namely best creep resistance) among all alloys compared. Only the RR350 (Al-4.8Cu-0.17Zr-1.2Ni-0.26Co) alloy [14] showed the comparable lowest creep rates owing to the high Ni and Co contents in the alloy.
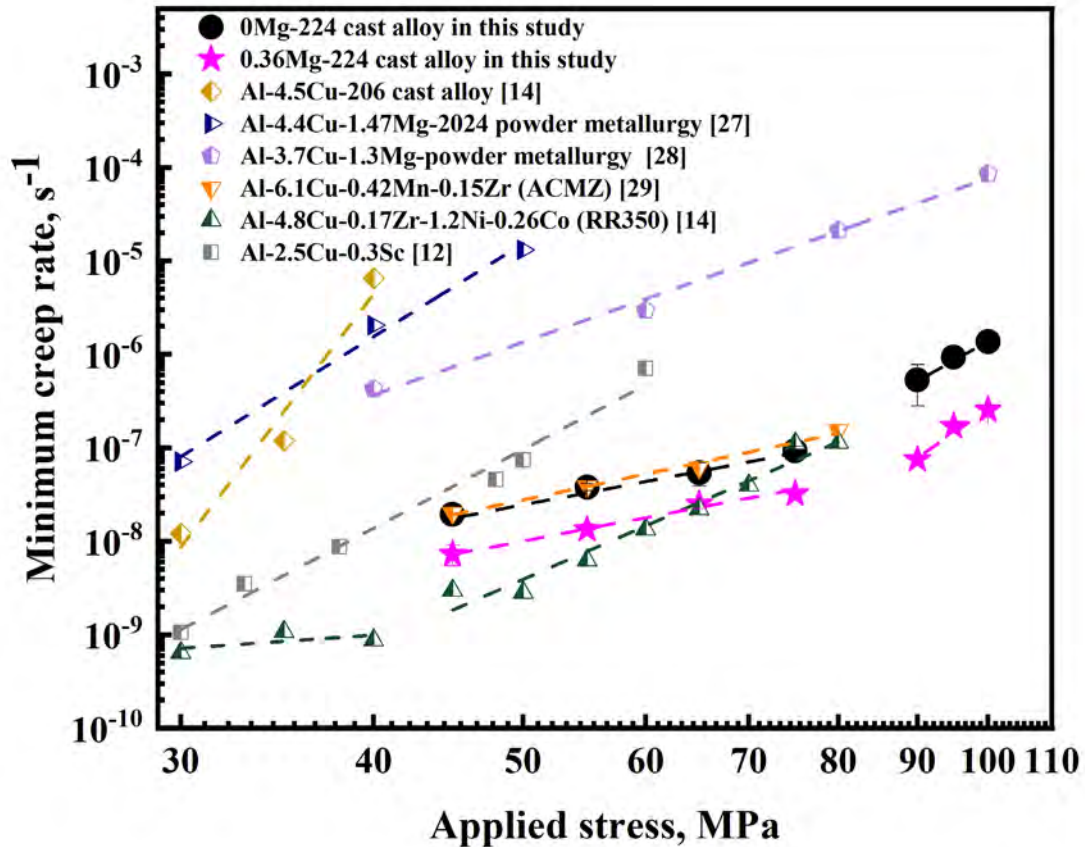
Fig. 15 Comparison of the minimum creep rates for various aluminum alloys; all tested at 300 °C.

5. Conclusions

1) Microalloying with Mg yielded finer and denser θ′ precipitates after T7A treatment relative to the Mg-free base alloy. The high coarsening resistance of the precipitates in the Mg-containing alloys improves the yield strength at both room temperature and 300 °C.

2) The addition of Mg improved creep resistance. With increasing Mg content, the total creep strain and minimum creep rates decreased, and the time to failure increased. Among the four alloys studied, the alloy with 0.36 wt% Mg exhibited the best creep resistance.

3) During creep deformation, the θ′ precipitates continued to coarsen in all four alloys. However, Mg microalloying significantly stabilized the θ′ precipitates in the matrix by slowing down the coarsening process of the precipitates, which improved the creep resistance of the alloys.

4) Two regimes were observed in the creep rate curves for all four alloys (that is, the LSR and HSR), and they were separated by a break with different stress exponents. The pronounced breaks revealed different creep mechanisms below and above the breaks: dislocation climbing in the LSR and Orowan looping in the HSR.

Data availability

The raw/processed data required to reproduce these findings cannot be shared at this time as the data also forms part of an ongoing study.

References

[1] M. Javidani, D. Larouche, Application of cast Al–Si alloys in internal combustion engine components, Int. Mater. Rev. 59 (2014) 132-158.
https://doi.org/10.1179/1743280413Y.0000000027
[2] J. Rakhmonov, K. Liu, L. Pan, F. Breton, X. G. Chen, Enhanced mechanical properties of high-temperature-resistant Al–Cu cast alloy by microalloying with Mg, J. Alloys Compd. 827 (2020) 154305.
https://doi.org/10.1016/j.jallcom.2020.154305
[3] P. Ramakrishnan, Automotive applications of powder metallurgy, Adv. Powder. Metall. Woodhead Publishing, (2013) 493-519.
https://doi.org/10.1533/9780857098900.4.493
[4] T. Nakajima, M. Takeda, T. Endo, Accelerated coarsening of precipitates in crept Al–Cu alloys, Mater. Sci. Eng. A 387 (2004) 670-673.
https://doi.org/10.1016/j.msea.2004.01.131
[5] L. Jin, K. Liu, X. G. Chen, Evolution of dispersoids and their effects on elevated-temperature strength and creep resistance in Al-Si-Cu 319 cast alloys with Mn and Mo additions, Mater. Sci. Eng. A 770 (2020) 138554.
https://doi.org/10.1016/j.msea.2019.138554
[6] D. Yao, W. Zhao, H. Zhao, F. Qiu, Q. Jiang, High creep resistance behavior of the casting Al–Cu alloy modified by La, Scripta Mater. 61 (2009) 1153-1155.
https://doi.org/10.1016/j.scriptamat.2009.09.007
[7] K. R. Athul, U. T. S. Pillai, A. Srinivasan, B.C. Pai, A review of different creep mechanisms in Mg alloys based on stress exponent and activation energy, Adv. Eng. Mater. 18 (2016) 770-794.
https://doi.org/10.1002/adem.201500393
[8] S. Mondol, S. Kashyap, S. Kumar, K. Chattopadhyay, Improvement of high temperature strength of 2219 alloy by Sc and Zr addition through a novel three-stage heat treatment route, Mater. Sci. Eng. A 732 (2018) 157-166.
https://doi.org/10.1016/j.msea.2018.07.003
[9] B. Rouxel, M. Ramajayam, T. J. Langan, J. Lamb, P.G. Sanders, T. Dorin, Effect of dislocations, Al3 (Sc, Zr) distribution and ageing temperature on θ′ precipitation in

Al-Cu-(Sc)-(Zr) alloys. Mater. 9 (2020) 100610.
https://doi.org/10.1016/j.mtla.2020.100610

[10] D. N. Seidman, E. A. Marquis, D. C. Dunand, Precipitation strengthening at ambient and elevated temperatures of heat-treatable Al (Sc) alloys, Acta Mater. 50 (2002) 4021-4035. https://doi.org/10.1016/S1359-6454(02)00201-X

[11] C. B. Fuller, D. N. Seidman, D. C. Dunand, Mechanical properties of Al (Sc, Zr) alloys at ambient and elevated temperatures, Acta Mater. 51 (2003) 4803-4814. https://doi.org/10.1016/S1359-6454(03)00320-3

[12] Y. H. Gao, C. Yang, J. Y. Zhang, L. F. Cao, G. Liu, J. Sun & E. Ma, Stabilizing nanoprecipitates in Al-Cu alloys for creep resistance at 300° C. Materials Research Letters, 7 (2019) 18-25. https://doi.org/10.1080/21663831.2018.1546773

[13] A. Shyam, S. Roy, D. Shin, J. D. Poplawsky, L. F. Allard, Y. Yamamoto, J. R. Morris, B. Mazumder, J. C. Idrobo, A. Rodriguez, T. R. Watkins, J. A. Haynes, Elevated temperature microstructural stability in cast AlCuMnZr alloys through solute segregation, Mater. Sci. Eng. A 765 (2019) 138279. https://doi.org/10.1016/j.msea.2019.138279

[14] B. K. Milligan, S. Roy, C. S. Hawkins, L. F. Allard, A. Shyam, Impact of microstructural stability on the creep behavior of cast Al–Cu alloys, Mater. Sci. Eng. A 772 (2020) 138697. https://doi.org/10.1016/j.msea.2019.138697

[15] M. Pekguleryuz, M. Celikin, Creep resistance in magnesium alloys, Int. Mater. Rev. 55 (2010) 197-217. https://doi.org/10.1179/095066010X12646898728327

[16] M. E. Kassner, Fundamentals of creep in metals and alloys, Butterworth-Heinemann, 2015.

[17] Y. Xu, L. Zhan, L. Xu, M. Huang, Experimental research on creep aging behavior of Al-Cu-Mg alloy with tensile and compressive stresses, Mater. Sci. Eng. A 682 (2017) 54-62. https://doi.org/10.1016/j.msea.2016.11.043

[18] C. Yang, L. Cao, Y. Gao, P. Cheng, P. Zhang, J. Kuang, J. Zhang, J. Sun, Nanostructural Sc-based hierarchy to improve the creep resistance of Al–Cu alloys, Mater. Des. 186 (2020) 108309. https://doi.org/10.1016/j.matdes.2019.108309

[19] W. S. Tian, Q. L. Zhao, Q. Q. Zhang, F. Qiu, Q. C. Jiang, Superior creep resistance of 0.3 wt% nano-sized TiCp/Al-Cu composite, Mater. Sci. Eng. A 700 (2017) 42-48. https://doi.org/10.1016/j.msea.2017.05.101

[20] R. Lagneborg, B. Bergman, The stress/creep rate behaviour of precipitation-hardened alloys, Met. Sci. 10 (1976) 20-28. https://doi.org/10.1179/030634576790431462

[21] R. A. Stevens, P. E. J. Flewitt, The dependence of creep rate on microstructure in a γ′ strengthened superalloy, Acta Metall. 29 (1981) 867-882. https://doi.org/10.1016/0001-6160(81)90129-2

[22] J. Rösler, E. Arzt, A new model-based creep equation for dispersion strengthened materials. Acta Metall. Mater. 38 (1990) 671-683. https://doi.org/10.1016/0956-7151(90)90223-4

[23] Y. H. Yeh, H. Nakashima, H. Kurishita, S. Goto, H. Yoshinaga, High-temperature creep and threshold stress of precipitation-hardened Al-0.7 at% Mn alloy, Mater. Trans. JIM 32 (1991) 52-60. https://doi.org/10.2320/matertrans1989.32.52

[24] B. Bergman, Creep deformation of two-phase Cu-Co alloys, Scand. J. Metall. 4 (1975) 177-181.

[25] M. Kerr, N. Chawla, Creep deformation behavior of Sn–3.5 Ag solder/Cu couple at small length scales, Acta Mater. 52 (2004) 4527-4535. https://doi.org/10.1016/j.actamat.2004.06.010

[26] S. Mitra, Elevated temperature deformation behavior of a dispersion-strengthened Al-Fe, V, Si alloy, Metall. Mater. Trans. A 27 (1996) 3913-3923. http://doi.org/10.1007/BF02595640

[27] L. Kloc, S. Spigarelli, E. Cerri, E. Evangelista, T.G. Langdon, Creep behavior of an aluminum 2024 alloy produced by powder metallurgy, Acta Mater. 45 (1997): 529-540. https://doi.org/10.1016/S1359-6454(96)00190-5

[28] L. Wang, F. Qiu, Q. Zhao, M. Zhao & Q. Jiang, Superior high creep resistance of in situ nano-sized TiCx/Al-Cu-Mg composite, Sci. Rep. 7 (2017) 4540. https://doi.org/10.1038/s41598-017-04816-0

[29] S. Bahl, J. Rakhmonov, C. Kenel, D. C. Dunand, A. Shyam, Effect of grain-boundary θ-Al2Cu precipitates on tensile and compressive creep properties of cast Al–Cu–Mn–Zr alloys, Mater. Sci. Eng. A 840 (2022) 142946. https://doi.org/10.1016/j.msea.2022.142946

[30] P. Hu, K. Liu, L. Pan, F. Breton, X. G. Chen, Evolution of precipitates and mechanical properties in Al-Cu 224 cast alloys with various Mg additions, COM 60th Conference of Metallurgists Proceedings, 00121 (2021) 105-114.

[31] P. M. Kelly, A. Jostsons, R. G. Blake, J. G. Napier, The determination of foil thickness by scanning transmission electron microscopy, Phys. Status. Solidi. A 31 (1975) 771-780. https://doi.org/10.1002/pssa.2210310251

[32] J. F. Nie, B. C. Muddle, Strengthening of an Al–Cu–Sn alloy by deformation-resistant precipitate plates, Acta Mater. 56 (2008) 3490-3501. https://doi.org/10.1016/j.actamat.2008.03.028

[33] S. Roy, L. F. Allard, A. Rodriguez, W. D. Porter, A. Shyam, Comparative evaluation of cast aluminum alloys for automotive cylinder heads: Part II: Mechanical and thermal properties, Metall. Mater. Trans. A Phys. Metall. Mater. Sci. 48 (2017) 2543-2562. http://doi.org/10.1007/s11661-017-3986-0

[34] D. Li, K. Liu, J. Rakhmonov, X. G. Chen, Enhanced thermal stability of precipitates and elevated-temperature properties via microalloying with transition metals (Zr, V and Sc) in Al–Cu 224 cast alloys, Mater. Sci. Eng. A 827 (2021) 142090. https://doi.org/10.1016/j.msea.2021.142090

[35] E. W. Andrews, J. S. Huang, L. J. Gibson, Creep behavior of a closed-cell aluminum foam Acta Mater. 47 (1999) 2927-2935. https://doi.org/10.1016/S1359-6454(99)00161-5

[36] H. J. Frost, M. F. Ashby, Deformation mechanism maps: the plasticity and creep of metals and ceramics, Pergamon press, 1982.

[37] J. Rösler, E. Arzt, The kinetics of dislocation climb over hard particles—I. Climb without attractive particle-dislocation interaction. Acta Metall. 36 (1988) 1043-1051. https://doi.org/10.1016/0001-6160(88)90158-7

[38] S. Mukherjee, M. Nuhi, A. Dasgupta, M. Modarres, Creep constitutive models suitable for solder alloys in electronic assemblies, J. Electron. Packag. 138 (2016) 030801. https://doi.org/10.1115/1.4033375

[39] W. Z. Han, A. Vinogradov, C. R. Hutchinson, On the reversibility of dislocation slip during cyclic deformation of Al alloys containing shear-resistant particles, Acta Mater. 59 (2011) 3720-3736. https://doi.org/10.1016/j.actamat.2011.03.007

[40] W. C. Oliver, W. D. Nix, High temperature deformation of oxide dispersion strengthened al and Al-Mg solid solutions, Acta Metall. 30 (1982) 1335-1347. https://doi.org/10.1016/0001-6160(82)90153-5

[41] J. da Costa Teixeira, L. Bourgeois, C. W. Sinclair, C. R. Hutchinson, The effect of shear-resistant, plate-shaped precipitates on the work hardening of Al alloys: towards a prediction of the strength–elongation correlation, Acta Mater. 57 (2009) 6075-6089. https://doi.org/10.1016/j.actamat.2009.08.034